

Nuclear surface studies with antiprotonic atom X-rays

S. Wycech¹, F.J. Hartmann², J. Jastrzębski³, B. Klos⁴, A. Trzcińska³, T. von Egidy²

¹ *Soltan Institute for Nuclear Studies, Warsaw, Poland*

² *Physics-Department, Technical University of Munich, Garching, Germany*

³ *University of Warsaw, Warsaw, Poland and*

⁴ *University of Silesia, Katowice, Poland*

(Dated: October 15, 2018)

The recent and older level shifts and widths in \bar{p} atoms are analyzed. The results are fitted by an antiproton-nucleus optical potential with two basic complex strength parameters. These parameters are related to average S and P wave scattering parameters in the subthreshold energy region. A fair consistency of the X-ray data for all Z values, stopping \bar{p} data and the $\bar{N}N$ scattering data has been achieved. The determination of neutron density profiles at the nuclear surface is undertaken, and the determination of the neutron R_{rms} radii is attempted. Uncertainties due to the input data and the procedure are discussed.

PACS numbers: PACS numbers: 13.75.Ev, 21.30.-x, 25.80.Pw, 36.10.Gv

I. INTRODUCTION

Recent CERN/LEAR measurements of X-ray transitions in antiprotonic atoms provide new data on the level shifts and widths in heavy systems [1]. These results complement older CERN, BNL and other [2, 3, 4] studies in medium Z atoms and fairly recent experiments with hydrogen, deuterium and helium [5, 6, 7, 8]. The main distinction of the new results from those obtained earlier in light nuclei is a much broader data basis, extended to the region of neutron excess and deformed nuclei. With the enlarged data one can attempt an extraction of a phenomenological \bar{p} optical potential that contains separate strengths of $p\bar{p}$ and $n\bar{p}$ interactions [9, 10]. It allows to study properties of the neutron density distributions at the nuclear surface. As stressed on many occasions the \bar{p} atoms are well suited for such studies. A problem is met on this way as the best description of the atomic data indicate the $p\bar{p}$ and $n\bar{p}$ absorption rates to be roughly the same. This result is in conflict with the chamber studies of low energy \bar{p} annihilation [11, 12]. The latter experiments indicate the $p\bar{p}$ absorption rate to be twice as fast as the $n\bar{p}$ one. This discrepancy has to be understood and we indicate the solution.

The content of this paper is as follows. In section II, the optical potential is constructed for \bar{p} bound into atomic states. It consists of two terms, the central and the gradient one. The strengths of these terms are phenomenological parameters which describe the S and P wave $\bar{N}N$ scattering amplitudes extrapolated below the $\bar{N}N$ threshold. The easiest way to learn about such amplitudes are the simple systems $^1,2\text{H}-\bar{p}$ and $^3,4\text{He}-\bar{p}$. Here, we rely on the absorptive amplitudes extracted from these atoms. Additional constraints follow from the chamber experiments [11, 12]. Some degree of unification of these data is obtained in terms of $\bar{N}N$ interaction potentials, in particular the recent updates of the Paris potential [13]. This allows for an approximate separation of the S and P wave absorption which is implemented into the optical potential.

The X-ray data from the four lightest atoms indicate the existence of two quasi-bound $\bar{N}N$ states. One state occurs in an S wave. It finds strong support in the $J/\psi \rightarrow \bar{p}p\gamma$ decays which allow to pinpoint its quantum numbers, [14]. The second quasi-bound state occurs in a P wave, [15], and so far has no independent confirmation. Both states are reproduced by the Paris model, [13], and this facilitates our discussion of the \bar{p} atoms.

Second question studied in Section II is the sensitivity of atomic levels and level widths to the nuclear densities. A significant dependence on the input charge densities is found. We attempt a model independent parametrization of the neutron densities and argue that \bar{p} atoms test nuclear surfaces but not the single particle asymptotic density regions.

The optical potential parameters are found via the best fit procedure to 117 atomic X-ray data. The fit is improved considerably by the effect of $\bar{N}N$ S wave quasi-bound state. The other, P wave, state is of no importance but it can explain anomalies observed in \bar{p} capture on loosely bound nucleons [16].

In a number of cases the atomic level widths may be rather precisely measured for two orbits per atom, the "lower" and the "upper" one. Such widths are useful to study properties of the nuclear surface. Atomic level shifts are less accurate and more difficult to understand. These difficulties reflect to a large extent the uncertainties in the understanding of basic $\bar{N}N$ interactions.

In section III, the R_{rms} radii of the neutron density distributions - R_{rms} - are extracted for several isotopes of Ca, Zr, Sn, Te and Pb. This is done on the basis of X-ray data and radiochemical measurements [17, 18, 19, 20] which test the ratios of neutron and proton densities in the region even more peripheral than that for the X-rays [21]. The radiochemical data determine the rate of $\bar{p}n$ capture relative to $\bar{p}p$ capture at very large distances. These are

discussed as a separate issue, since the nuclear region involved in this process is located about 1 fm farther away from the region tested by the atomic X-rays. Most of the effort is devoted to the evaluation of uncertainties involved in this method of density determination.

The appendix discusses some details of the gradient potential.

The present publication addresses also three more specific questions:

- The optical potential for antiprotons involves uncertain quantities: the range and strengths of the $\bar{N}N$ interaction and nuclear densities at large distances. Errors due to these uncertainties on the atomic level widths are evaluated.
- The experimental level widths in heavy atoms are determined by high moments of the neutron density. However, the nuclear structure physics is more interested in the low moments, in particular in the rms radius. How well could we determine the latter?
- Can antiprotonic data distinguish a neutron skin from a neutron halo as defined in Ref. [22]?

A number of phenomenological optical potentials have been fitted to the \bar{p} X-ray data. Recent results may be found in Refs. [9, 10]. The present work is different in several aspects:

- We include recoil effects in the P wave $\bar{N}N$ interactions.
- The constraints from $Z = 1$, $Z = 2$ atoms, \bar{p} absorption in flight and $\bar{N}N$ potential models are accounted for.
- The data set is larger.

The constraints allow to obtain the absorptive optical potential parameters close to those expected from the $\bar{N}N$ scattering data. In consequence a good fit to the atomic X-ray data is obtained.

II. THE OPTICAL POTENTIAL

Atomic energy levels of antiprotons are determined essentially by the Coulomb and fine structure interactions. In addition, the \bar{p} -nucleus interactions generate level shifts ϵ and \bar{p} annihilation generates level broadenings Γ . Both effects may be conveniently described by a complex nuclear optical potential. The standard potentials, well tested for π atoms [9], are composed of two terms

$$V^{opt} = \sum_{p,n} [V_S(r) + \nabla V_P(r)\nabla] = V_S + \hat{V}_P, \quad (1)$$

with the sum extending over protons and neutrons. Both terms, the local V_S and the gradient V_P are expected to have a folded form

$$V_{S,P}(r) = \frac{2\pi}{\mu_{\bar{N}N}} a_{S,P} \int d\mathbf{u} g_{S,P}(\mathbf{u}) \rho(\mathbf{r} - \mathbf{u}), \quad (2)$$

where $\mu_{\bar{N}N}$ is the $\bar{N}N$ reduced mass and ρ is the nuclear density. Here a_S is expected to resemble the spin averaged S wave scattering length and a_P the P wave scattering volume. Two profile functions $g_{S,P}$, normalized by $\int d\mathbf{u} g_{S,P}(\mathbf{u}) = 1$, reflect the range of interactions. The $\bar{N}N$ annihilation radius r_o is expected in the range 0.8 – 1.0 fm. Such values follow from phenomenological or quark models of $\bar{N}N$ interactions. The effective annihilation radius in models with much shorter annihilation potentials is similar [13]. On the other hand, the ranges involved in $\text{Re } V_S$ and $\text{Re } V_P$ may be different. In this work, the same interaction range is assumed for all the components, and it is left as a free parameter. A Gaussian profile g is used.

The form of V^{opt} given in eq.(1) is related to the parametrization of the low energy scattering amplitudes

$$f = a_S + 3\mathbf{p}\mathbf{p}'a_P \quad (3)$$

where \mathbf{p}, \mathbf{p}' are the relative momenta of the colliding particles before and after the collision. An important distinction between $\bar{N}N$ and πN cases is that in the $N\bar{N}$ collisions the nucleon recoil effect is important and the relative momentum is $\mathbf{p} = (\mathbf{p}_N - \mathbf{p}_{\bar{N}})/2$. It involves the nucleon \mathbf{p}_N and antiproton $\mathbf{p}_{\bar{N}}$ momenta in equal proportions. As a consequence, gradients over nucleon wave functions arise in the optical potential. One needs a formula that generalizes eq.(1). The scattering amplitude (3) leads now to a new form of the gradient potential

$$\hat{V}_G(\mathbf{r}) = \frac{2\pi}{\mu_{\bar{N}N}} a_P \frac{3}{4} \sum_{\alpha} \int d\mathbf{r}' \varphi_{\alpha}^*(\mathbf{r}') (\overleftarrow{\nabla}_N - \overleftarrow{\nabla}_{\bar{N}}) f_P(\mathbf{r} - \mathbf{r}') (\overrightarrow{\nabla}_{\bar{N}} - \overrightarrow{\nabla}_N) \varphi_{\alpha}(\mathbf{r}') \quad (4)$$

where φ_α are the nucleon wave functions. The summation over nucleon states α and the integration over nuclear coordinates \mathbf{r}' are to be performed. This leads to a three-term expression for V_G

$$\hat{V}_G = \hat{V}_P + V_N + V_{mix} \quad (5)$$

and

$$V^{opt} = \sum_{p,n} [V_S + \hat{V}_G]. \quad (6)$$

The first term in Eq. (5) corresponds to the standard gradient potential, V_N is due to the gradients over nucleon functions, while V_{mix} follows from mixed nucleon and antiproton derivatives. In the states studied in experiments the nucleon dependent part $V_N + V_{mix}$ contributes about half of the V_G strength, and amounts to a quarter of the total V^{opt} . On a phenomenological level these two terms could be included into the V_S potential term. However, the difference arises when one attempts to relate a_S and a_P to the scattering data. A special effect comes from the dependence of these terms on the state of the nucleus, in particular on the angular momentum in the valence shells. In addition the mixing term may induce some nucleon-antinucleon correlations in odd-A nuclei. A more detailed discussion of the gradient terms is given in Appendix A, where some approximations are also introduced.

A. The choice of nuclear charge densities

The nuclear charge densities are well determined in the region of the nuclear surface between $c - 2a$ and $c + 2a$, where c is the half density radius and a is the surface diffuseness. These are the results of electron scattering and muonic atom experiments [23, 24]. However, the antiprotonic atoms involve also lower nuclear densities. In Fig.1 are shown the average radii of \bar{p} absorption in the "lower" atomic orbits. At those radii the nuclear charge densities amount to 5% of the central density. For the "upper" levels these radii are larger by 0.2 – 0.4 fm and involve charge densities smaller by a factor of 2. The absorption regions are localized in nuclear layers of about 3 fm radial depth. In these regions, the charge densities are not well known. To indicate the uncertainty, let us compare the relevant moments of several charge distributions. Atomic level widths in very high l orbits are given by expectation values $\Gamma/2 \simeq \langle n, l | V^{opt} | n, l \rangle$ where l is the angular momentum and n the principal quantum number of an atomic state. For large Bohr radii and weak nuclear absorption, the widths are proportional to $\langle r^{2l} \rangle$, the $2l$ -th moment of the nuclear density distribution. This reflects the dominant effect of high centrifugal barriers. In the states actually tested the finer details of the \bar{p} wave functions are significant and the dominant moments are $\langle r^{2l-2} \rangle$ and $\langle r^{2l-4} \rangle$. Several relevant moments of nuclear charge density are compared in Table I. For a given isotope, all charge density profiles yield essentially the same rms values. However, the moments of interest may differ by up to 30% in the highest observable l states. In particular the many-parameter multi-Gaussian density parametrization offer much shorter tails. Other extreme cases are given by some three-parameter Fermi distributions which often generate unrealistically low (and even negative) densities at very large distances. To select the "best" charge profile we follow the "averaging procedure" outlined in Ref. [25] for hyperonic atoms. Thus, the lowest moments $\langle r^2 \rangle$, $\langle r^4 \rangle$, $\langle r^6 \rangle$ are compared for several available charge profiles (Fermi, Gaussian, multi-Gaussian) and an average density in the sense of average moments is extracted. In the cases of Al, S, Ca, Pb, studied in Ref. [25] one always finds the average to be the closest to the profiles given in the most recent compilation by Fricke *et al* [24]. The same is found in all Ni, Zr and Sn isotopes studied here. We use the parameters of Ref. [24] as the basis of our calculations. The only exception is ^{16}O , where the sum of Gaussians and the deformed nuclei U, Th, where monopole density component were used [23]. Later, in specific cases, the comparison with other densities is presented.

B. The parametrization of nuclear densities

To understand the \bar{p} atomic data, one needs a reliable extrapolation of the densities to very large distances. The related problems are visualized in Fig.2. For two Ca isotopes the densities were calculated with a HFB-SkP model [26], and fitted at large distances by a two-parameter Fermi profile

$$\rho(r) = 1/(1 + \exp[(r - c)/a(r)]). \quad (7)$$

Instead of a constant diffuseness one has to introduce certain functions $a(r)$, which are plotted in Fig. 2. The dependence on radial distance is rather distinct. There are clear advantages of the 2pF profile, but with a constant a it does not reproduce the density in far away regions. That result is also fairly model independent and the shapes of $a(r)$ in Fig. 2 indicate a certain degree of universality. At distances $c + 3a \leq r \leq c + 6a$ one finds essentially the same

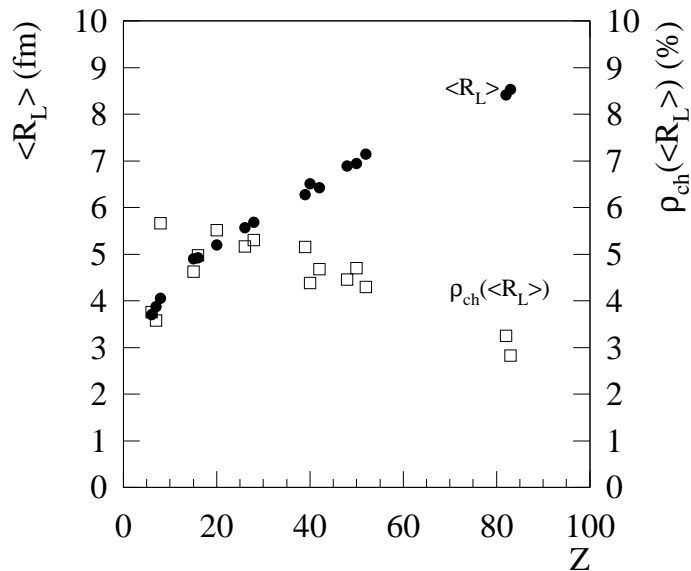


FIG. 1: Dots - the average antiproton absorption radii $\langle R_L \rangle$ (weighted by $\psi_{atom}^2 \text{Im } V^{opt,r^2}$) calculated for the "lower" atomic level, left scale in fm. Squares - the charge densities at these points, given on the right scale as % of the central charge densities. The bottom scale - atomic numbers Z . Calculations are done with densities from Ref. [24].

slope of $a(r)$ for a wide range of nuclei in Hartree-Fock, Hartree-Fock-Bogolubov [21, 26] and Relativistic Mean Field calculations [27]. However, at radii beyond this region, different nuclear models may produce different behavior.

The average annihilation radii r_a in Ca are marked by arrows. In the lower and upper states one has $r_a = 4.9$ fm and 5.3 fm respectively and $a(r)$ is seen to be fairly stable at these ranges. However, the radiochemical data involve larger radii from ≈ 5.1 fm up to $r \approx 7.5$ fm [21]. The diffuseness parameter $a(r)$ is seen to fall down in this region. The difficulty involved in the radial dependence of $a(r)$ is moderated by the optical potential which involves folded densities. With the folding range of ≈ 1 fm the corresponding downfall of $a_{folded}(r)$ is pushed away by ≈ 0.5 fm.

In order to understand $a(r)$ the first question to answer is where the single particle asymptotic limit is reached and what is its form. For a single neutron of angular momentum L bound in an external potential the asymptotic wave function is described by

$$\varphi_\alpha \sim h_L(irk_\alpha) = \frac{\exp(-rk_\alpha)}{r} W_L\left(\frac{1}{k_\alpha r}\right) \quad (8)$$

where $k_\alpha = \sqrt{2m_N E_\alpha}$, E_α is the neutron binding energy and W_L is a polynomial given by the Hankel function of order L (see e.g. [28]). This wave function allows to scale the asymptotic density $\rho(r) = \varphi_\alpha(r)^2$. The ratio of two densities $\rho(r)/\rho(r_o)$, taken at two points r_o and r , allows to find

$$\frac{1}{a(r)} = \left[\frac{1}{a(r_o)} - 2k_\alpha + 2 \ln\left(\frac{W_L(r_o)r}{W_L(r)r_o}\right) \right] \frac{r_o}{r} + 2k_\alpha. \quad (9)$$

This formula reproduces the shapes of $a(r)$ in the region of $r \approx 5 - 8$ fm with $k_\alpha \approx 1.25 \text{ fm}^{-1}$ which corresponds to $E_\alpha \approx 30 \text{ MeV}$. On the other hand, the separation energies are respectively 16 MeV (^{40}Ca) and 10 MeV (^{48}Ca). Thus the "true" single particle asymptotic density given by valence neutrons begins farther away. The second observation is that the effective k_α , which reproduces Fig. 2, corresponds to bindings larger than the average binding weighted by contributions of neutron orbitals to the total neutron density. The behavior of a nucleon at large distances involves virtual excitations of the residual system and a sizable fraction of k_α is due to the nuclear correlations. Contrary to a frequently expressed belief, the radii tested by antiprotons do not represent the far away distances of single particle asymptotic wave functions, and in this sense are more interesting for the nuclear structure research.

In practical terms the shortcomings of constant a can be corrected by the $a(r)$ given by eq. (9) with $k_\alpha \approx 1.25 \text{ fm}^{-1}$. Because of the large value of k_α the result is in practice independent of the value of L . Relation (9) is used here to interpolate between two values of the diffuseness parameter. The initial value $a(r_o)$ taken at $r_o = c + 3a$ is due to the full complexity of the nuclear structure which includes the average field and effects of nuclear correlations. It is kept as a free parameter, *the a*, to be determined from experiments and reproduced by models. Such a procedure serves only as a guiding principle for the best correlation of the atomic X-ray data and the radiochemical data. With

TABLE I: Moments $\langle r^{2l} \rangle = \int d\mathbf{r} \rho(\mathbf{r}) \mathbf{r}^{2l} / \int d\mathbf{r} \rho(\mathbf{r})$ of the charge density profiles in $10^{2l-3} \text{ fm}^{2l}$ units. The densities based on μ atom data -first column, electron scattering data - other columns: 2pF - two parameter Fermi, HO - harmonic oscillator, SOG - multigaussian.

Atom	moment	2pF(μ) [24]	2pF(e) [23]	HO(e) [23]	SOG(e) [23]
^{16}O	rms	2.72	2.72	2.72	2.71
	$\langle r^4 \rangle$	9.0	8.7	8.2	8.4
	$\langle r^6 \rangle$	1.6	1.5	1.2	1.3
^{32}S	rms	3.28	3.25		3.26
	$\langle r^4 \rangle$	17.2	16.9		1.69
	$\langle r^6 \rangle$	3.75	3.81		3.82
^{58}Ni	rms	3.79	3.78		3.77
	$\langle r^6 \rangle$	7.5	7.6		6.7
	$\langle r^8 \rangle$	2.6	2.5		1.9
^{116}Sn	rms	4.64	4.65		4.63
	$\langle r^8 \rangle$	8.6	9.8		7.9
	$\langle r^{10} \rangle$	4.2	5.1		3.7
	$\langle r^{12} \rangle$	2.5	3.3		1.7
^{124}Sn	rms	4.68	4.66		4.69
	$\langle r^8 \rangle$	9.3	9.5		8.4
	$\langle r^{10} \rangle$	4.6	4.8		3.7
	$\langle r^{12} \rangle$	2.6	2.9		1.8
^{208}Pb	rms	5.504	5.520		5.503
	$\langle r^{12} \rangle$	11	13		9.3
	$\langle r^{14} \rangle$	8.7	11.2		6.2

an improved optical potential and more precise data it should be repeated with specific nuclear models. However, at this stage the proper choice of $a(r_o)$ and the form of the proton (charge) densities are more urgent questions.

C. Constraints on the optical potential parameters

The $N\bar{N}$ amplitudes of eq.(3) are related to the amplitudes tested in scattering experiments. The latter extrapolated to the $N\bar{N}$ threshold yield scattering lengths and scattering volumes which parametrize the low energy scattering. The relation of the experimental lengths and volumes to those required in the optical potential is not direct: first - $a_S(E)$ and $a_P(E)$ are strongly energy dependent and one needs these amplitudes for bound particles and second - some nuclear many body corrections may arise. An additional difficulty is related to the large number of $N\bar{N}$ partial waves involved, and at this stage of research one can operate only with the spin averaged values. So far, the safest method to find the optical potential was to extract the potential parameters from the best fit to the atomic data [9, 10]. In our work we adopt a mixed procedure: the parameters are semi-free, subject to constraints from other experiments. In addition, we are guided by the Paris model of $N\bar{N}$ interactions.

At the nuclear surface \bar{p} may interact with quasi-free but bound nucleons. In the $N\bar{p}$ system the relevant energy is negative since both particles are bound and some recoil energy is taken away by the relative motion of the $N\bar{p}$ pair with respect to the residual $A - 1$ nucleons. Hence, one needs to know the amplitude f below the $N\bar{p}$ threshold

$$f = a_S(-E_B - E_{rec}) + 3\mathbf{p}\mathbf{p}' a_P(-E_B - E_{rec}) \quad (10)$$

where E_B is the sum of antiproton and nucleon separation energies and $E_{rec} = p_{rec}^2/2\mu_{rec}$ is the recoil energy. The distribution of the recoil momenta - p_{rec} - is calculable from the Fourier transforms of the antiproton and nucleon wave functions $\Psi_{\bar{p}}(\mathbf{r})\varphi_N(\mathbf{r})$. In practice, such calculations can be done easily in the lightest atoms: deuterium and helium [29]. In the "lower" ($l = 0$) and "upper" ($l = 1$) orbitals of ^2H \bar{p} atoms one obtains average values $\langle E_{rec} \rangle = 9$ and 4 MeV respectively. In heavier nuclei such calculations are less reliable but the spectrum of p_{rec} was measured with \bar{p} stopped in Ne streamer chamber [30]. The p_{rec} distribution peaks at ≈ 180 MeV and gives $\langle E_{rec} \rangle \approx 11$

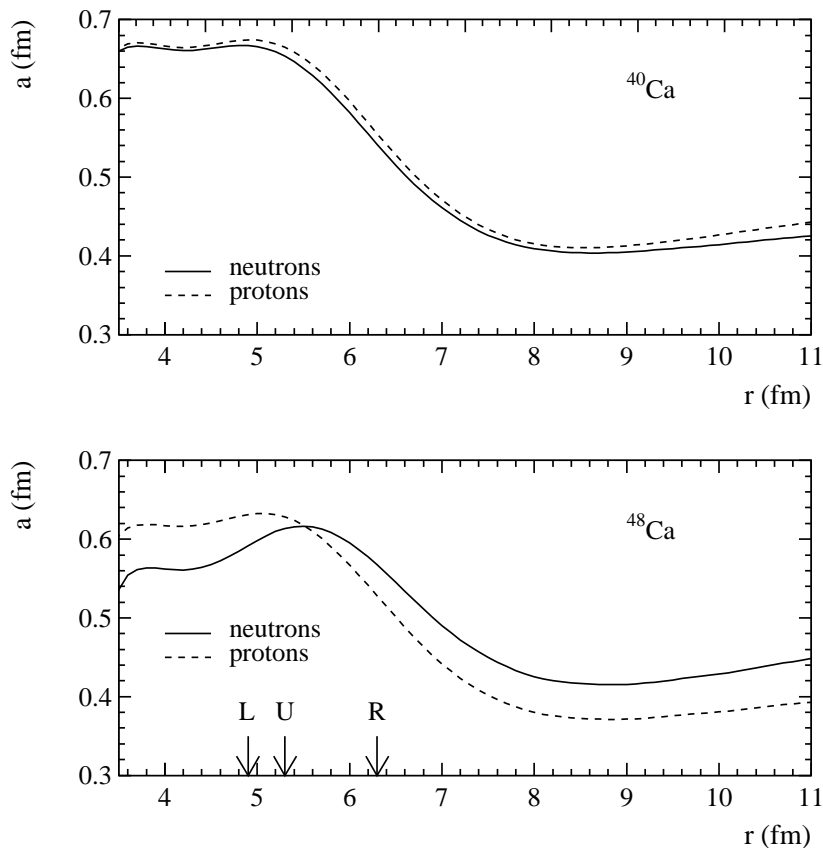


FIG. 2: The proton and neutron densities in two Ca isotopes calculated in a HFB shell model have been approximated by the two parameter Fermi distribution with constant c and variable $a(r)$. Functions $a(r)$ are plotted to show its asymptotic behavior at large distances. The arrows indicate absorption radii for the lower (L), upper (U) and radiochemical (R) experiments, correspondingly.

MeV. This value is used in further calculations. In addition, we estimate a 5 MeV difference of $\langle E_{rec} \rangle$ in the "lower" and the "upper" atomic state.

The energy dependence of the $N\bar{p}$ scattering amplitudes in the sub-threshold region may be obtained, to some extent, from the ^1H , ^2H , ^3He , ^4He atoms since the nucleon separation energies in these nuclei span the region from 0 to 21 MeV. Calculations based on the multiple scattering series summation from Ref. [29] and data from Refs. [5, 6, 7, 8], are presented in Fig. (3). From the level shifts and widths in these elements one can extract averaged absorptive parts of $\text{Im } a_S$ and $\text{Im } a_P$ via a best fit procedure [15]. The nucleon binding energies characteristic for surfaces of large nuclei locate the $E_B + E_{rec}$ energies in the sector (40 to 15) MeV. Corresponding values of $\text{Im } a_S$ and $\text{Im } a_P$ indicate the strengths of the absorptive optical potentials expected in nuclei. Two results are of significance in the analysis of the optical potential. First, the S -wave absorption strength $\text{Im } a_S$ increases with the decreasing energy. The physics behind it is related to a broad quasi-bound $N\bar{N}$ state which is indicated by the atomic data and generated by the Paris potential. Its existence is also inferred from the $\bar{p}p$ correlations observed in $J/\psi \rightarrow \bar{p}p\gamma$ decays, [14]. The impact of such phenomenon is discussed in the next section, it is clearly seen in the comparison of "lower" and "upper" widths. Second, a resonant-like behavior arises in a P -wave close to -10 MeV. Figure (3) indicates that a similar effect is also generated by the Paris potential model, where it is attributed to the iso-triplet, spin-singlet 3P_1 quasi-bound state. It affects antiproton capture on very loosely bound nucleons [16].

A different constraint on the isospin structure of $\text{Im } a_S$ follows from studies of π mesons produced by \bar{p} stopped in chambers [11, 12]. These experiments yield ratios of annihilation rates $R_{n/p} = \sigma(\bar{p}n)/\sigma(\bar{p}p)$ given in Table II. Since the \bar{p} are stopped in light elements the interaction involves S waves and the cross sections are related to the absorptive amplitudes $\sigma(N\bar{p}) \sim \text{Im } a_S(N\bar{p})$ for the $n\bar{p}$ and $p\bar{p}$ pairs, respectively. Inspection of Fig. (3) shows that the $R_{n/p}(S)$ for the S waves is well reproduced by the Paris potential model. The same model predicts $R_{n/p}(P) \approx 1$ for the average of P waves at energies of our main interest. These constraints are considered as possible improvements of our optical potential. It turns out that the condition $R_{n/p}(P) \approx 1$ is consistent with the atomic data. In this respect our results follow the findings of Ref. [10]. The chamber result $R_{n/p}(S) \approx 0.5$ leads to no or a marginal improvement

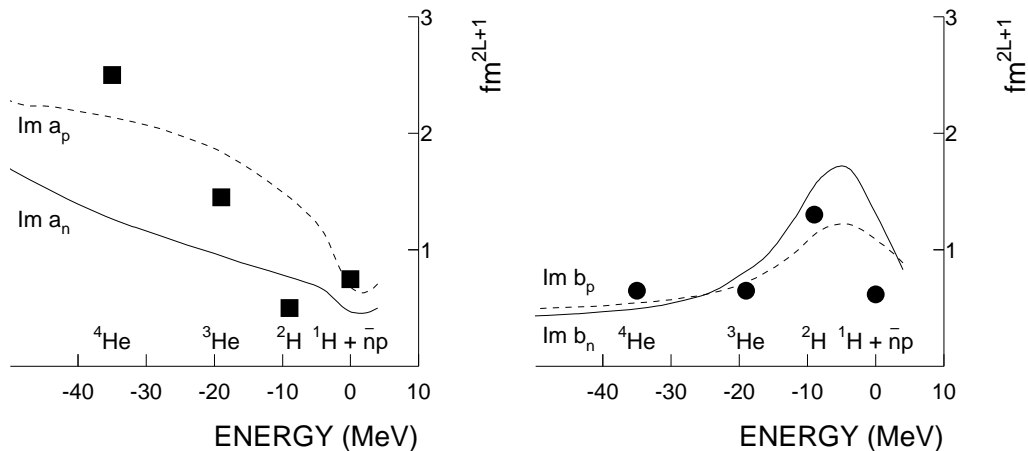


FIG. 3: Left panel: the absorptive parts of $\bar{p}N$ S -wave amplitudes in the sub-threshold region extracted from the atomic level shifts and widths in ${}^1\text{H}$, ${}^2\text{H}$, ${}^3\text{He}$, ${}^4\text{He}$. $\text{Im } a_S(E)$ averaged over spins and isospin of the nucleons are given by squares located at the corresponding values of $E_B + \langle E_{rec} \rangle$. The curves are calculated with the recent updates of Paris NN potential, [13]. The dotted lines refer to $p\bar{p}$ and the continuous lines to $n\bar{p}$ systems. Right panel: the absorptive parts of $\bar{p}N$ P -wave amplitudes in the sub-threshold region extracted from the atomic level shifts and widths in ${}^1\text{H}$, ${}^2\text{H}$, ${}^3\text{He}$, ${}^4\text{He}$ (circles) The curves – Paris potential calculations.

over that for $R_{n/p}(S) \approx 1$. On the other hand, it changes the neutron density radii extracted from \bar{p} atoms.

TABLE II: The experimental antiproton capture ratios $R_{n/p} = \sigma(\bar{p}n)/\sigma(\bar{p}p)$ extracted from capture in flight.

Element	$R_{n/p}$	reference
${}^2\text{H}$	0.81(3)	[11]
${}^3\text{He}$	0.47(4)	[12]
${}^4\text{He}$	0.48(3)	[12]

D. The constrained best-fit potential

An overall best fit to the 117 atomic data was performed. It includes measurements in N, C, O, P, S, Cl, Ca, Fe, Co, Ni, Y, Zr, Cd, Mo, Sn, Te, Pb, Bi, Th and U, in total 37 isotopes. Several precise results were excluded: ${}^6,7\text{Li}$ - as the optical potential may not be well applicable there, ${}^{18}\text{O}$ - due to the large uncertainty of the charge density profile as exemplified already in ${}^{16}\text{O}$, Yb - due to its uncommon deformation. An anomalous lower width in ${}^{58}\text{Fe}$ was dropped and several very old and uncertain results have not been considered.

One cannot find the best fit parameters jointly with the details of uncertain neutron densities in each individual isotope. To obtain an overall best fit the following strategy was adopted. An overall trend of the neutron rms radius as a function of the neutron excess $\delta = (N - Z)/(N + Z)$ was assumed and for $Z > 10$ a linear interpolation was tried. Two such trends were fitted before to the atomic \bar{p} data. One, called "hadronic" is indicated by the hadronic scattering data [31]

$$\Delta R_{np} \equiv R_{rms}(n) - R_{rms}(p) = -0.09(2) + 1.46(12) \delta. \quad (11)$$

It is close to the trend obtained by Friedman *et al* as a result of pionic atom data and the best-fit to the antiproton X-ray data [10]. Another "atomic" trend follows from the \bar{p} atomic data analyzed with zero $\bar{N}N$ annihilation range and $R_{n/p} = 1$, [32],

$$R_{rms}(n) - R_{rms}(p) = -0.03(2) + 0.90(15) \delta \quad (12)$$

Both slopes can be supported by nuclear model calculations and it is appropriate at this point to remind that nuclear models are not able to predict the neutron radii and we have to fit some parameters to experimental data. This point is particularly strongly stressed by Furnstahl [33] and a similar point of view is taken in the recent extensive calculation by Ring *et al.* [27]. Neither of these trends indicated above needs to be true, some nuclei lie far away from

the averages given above. Here, we use the slope to get an initial insight into the best fit possibilities. Next with the best parameters for the optical potential, we find the best results for the neutron excess in some nuclei. This is done, following the procedure of Ref. [22], in terms of free neutron diffuseness a_n (neutron halo, $c_n = c_p$) or neutron half-density parameter c_n (neutron skin, $a_n = a_p$). An additional question is whether the inclusion of extra data, the radiochemical measurements or other experiments, determines some correlation of these two parameters.

TABLE III: Overall parameters for the optical potential fitted to atomic data: 78 - lower level shifts and widths, 39 - upper level widths. In the first line the slope follows eq.12. With other "hadronic" cases the slope was varied but close to the one given by eq.11. The best result is obtained with $\Delta R_{np}^h = -0.10(2) + 1.65(5)\delta$. The r_{rms} denotes the root mean square radius of the folding Gaussian profile. All charge densities come from Ref. [24]. Factor $f_i = 4/3$ for protons and $2/3$ for neutrons describes the chamber result, a_n or c_n denotes the neutron density free parameter.

"slope"	parameter	data	χ^2	χ^2/N	a_S [fm]	a_P [fm ³]	r_{rms} [fm]
Eq.12	a_n	all	293	2.50	-1.70 - 0.95i	-.01 - 0.39i	0.80
ΔR_{np}^h	c_n	all	285	2.43	-1.70 - 0.95i	-0.0 - 0.35i	0.79
ΔR_{np}^h	a_n	all	262	2.24	-1.65 - 0.85i	-0.0 - 0.41i	0.79
ΔR_{np}^h	a_n	all	262	2.24	-1.60 - $f_i 0.95i$	-0.0 - 0.39i	0.79
ΔR_{np}^h	a_n	lower	160	2.24	-1.60 - 0.95i	-0.0 - 0.41i	0.79
ΔR_{np}^h	a_n	upper	87	2.05	-1.60 - 0.62i	-0.0 - 0.41i	0.79

The initial best fit results are given in Table III. The faster ΔR_{rms} slope deduced from the hadronic scattering offers a better χ^2 . This result differs from the result obtained in ref. [32], as it is based on both widths and level shifts while ref. [32], used level widths. The best result $\Delta R_{np} = -0.10(2) + 1.65(5)\delta$ obtained with a change of the diffuseness parameter a_n corresponds to line 4 in Table III. The difference of our result and that given by eq.(11) and Ref. [10] is due mainly to the input charge densities. Here, the more recent muon-based data [24] are used while results of Ref. [10] are based mainly on the electron data. As discussed in previous sections and indicated in Table I, the muonic data are close to the "average" results and in this sense seem to be preferable. In addition,

Another minimum of χ^2 is obtained with changes of the half-density radius c_n at a very high slope $\Delta R_{rms} = -0.10 + 2.0 \delta$. Although the total χ^2 is much worse in this case, it turns out to be better for some specific isotopes. This question is discussed in the next section. Let us also notice that the best potential parameters are fairly close for both the "atomic" and the "hadronic" slopes.

The preference found in chamber experiments [11, 12] for a stronger S wave annihilation on protons, $R_{n/p}(S) \approx 0.5$, is now introduced into the optical potential parameters. The effect is given in line 4 of Table III. It does not change the best fit, but is accepted by the data. It is also weakly reflected in the analysis of radiochemical data as the absorption in P waves is dominant. The effective ratio of the absorption rates $R_{n/p}$ depends on the partial wave in the antiproton-nucleon system. For each atomic state the mixture of S and P wave is slightly different. We calculate a kind of average value characteristic for all Z, n, L states considered in this analysis. For the best fit potential of table IV one obtains $R_{n/p} = 0.86(4)$ as the best average representation for the capture ratio $\sigma(\bar{p}n)/\sigma(\bar{p}p)$ at large distances tested in the radiochemical experiments. The uncertainty given in parentheses describes the dispersion of $R_{n/p}$ obtained in this way. A more detailed discussion of this point may be found in Ref. [34].

Lines 5 and 6 in Table III give separate best fits to the lower and upper levels. To find the best solution on those limited data sets only $\text{Im } a_S$ was varied. The motivation for such a choice comes from the shape $\text{Im } a_S(E)$ in Fig.(3). The best fit absorptive parts compare well with the values of $\text{Im } a_S(E)$ at the characteristic subthreshold energies of about -30 MeV.

TABLE IV: The best fit potential based on X-ray data, consistent with the chamber experiments, the lightest atoms and the $N - \bar{N}$ Paris potential. $f_i = 4/3$ for protons and $2/3$ for neutrons. a_S ("upper") is to be used for the upper levels and a_S ("lower") for the lower ones.

χ^2	χ^2/N	a_S ("upper")[fm]	a_S ("lower")[fm]	a_P [fm ³]	r_o [fm]
247	2.11	-1.60 -i 0.74 f_i	-1.60 - i 1.10 f_i	-0.0 - i0.39	0.79

Certain incompatibility in the description of lower and upper widths was noticed already in Ref. [9]. This effect is also reproduced here and it is indicated in Table III. The upper levels require weaker absorption and the explanation comes from the left panel of Fig.(3). The \bar{p} in the upper level encounters less-bound nucleons and the recoil energy is

also smaller. As discussed above, one expects the difference in recoil of some 5 MeV and the difference in the average bindings of some 3 MeV. The central energy involved in $a_{S,P}(-E_B - E_{rec})$ amounts to about - 35 MeV in the lower levels and about - 27 MeV in the upper levels. The total 8 MeV energy shift in the argument of $\text{Im } a_S(E)$ may reduce its value by 0.4 fm as required by the X-ray data. Table III indicates that such a change reduces the total χ^2 from 262 to 247. The final results are summarized in Table IV. This potential does not offer the best fit to the data, however it offers the best fit under the chamber constraint on the S wave absorption $R_{n/p}(S) = 0.5$. Relaxing this condition one can improve the total χ^2 by 2-3 units. In addition, it is possible to improve the fit to the data by relaxing the other condition $R_{n/p}(P) = 1$. There is no direct experimental indication for this P wave constraint, we are motivated entirely by the Paris potential calculations.

III. THE NEUTRON RADII

The differences of neutron and proton mean square radii, extracted from from several atoms, are given in Tables V and VI. These results indicate two basic problems:

First, the extracted $R_{rms}(n) - R_{rms}(p)$ depend rather strongly on the charge density input. In particular, the results in the Sn isotopes depend on the $\langle r^{12} \rangle$ moments dominating the upper level width. For two charge profiles in $^{112,116,120,124}\text{Sn}$: one from Ref. [23](electron scattering) and the other from Ref. [24](μ atoms) the ratios $\langle r^{12} \rangle_e / \langle r^{12} \rangle_\mu$ are : 1.63, 1.32, 1.42, 1.09, respectively. These differences reflect on the differences in neutron radii extracted from the antiproton data. As discussed above, the charge densities given by Fricke *et al* [24] are close to "average" densities generated in several μ atom and electron scattering experiments. In this sense these results are more likely than the others.

Second, the minimum χ^2 in each isotope was obtained either by enhancing the diffuseness parameter a_n or half density radius c_n . In most cases both minima offer good $\chi_{pdf}^2 \approx 1$ and additional data are required to determine the nuclear surface shape. However, in ^{112}Sn , ^{116}Sn , ^{90}Zr and ^{208}Pb the fit is bad and $\chi_{pdf}^2 \approx 3$. The discrepancy comes from the level shifts. In these cases the change of the half-density radius offers better χ^2 and such case is given in Table VI for Pb. The neutron radii obtained via the c_n extension are excessively large and run into conflict with most of the other data. We exemplify this situation in the case of Sn and Pb atoms, but it is typical to other large nuclei. In the Pb nucleus the two minima for $R_{rms}(n) - R_{rms}(p)$ yield very different results. The solution obtained by enlarging a_n is close to the results obtained in (p,p') scattering experiments [35]. Presumably it is the one that is physically acceptable. The uncertainty related to the charge density input is rather large but again there are good reasons to favor the last column based on the Ref. [24]. It is interesting to note that the second solution characterized by the extension of c_n and large difference $R_{rms}(n) - R_{rms}(p)$ of 0.5 fm is close to the result first obtained in the neutron/proton pickup experiment of Koerner and Schiffer [36]. This solution, if it represents the reality, has an interesting astrophysical significance [33].

The same interpretation follows from the results obtained in Sn. The neutron radii obtained with enhanced a_n are close to those obtained in the proton scattering experiment [37] that yields $R_{rms}(n) - R_{rms}(p) = 0.25(5)$ fm in ^{124}Sn , larger than 0.18(7) extracted via the dipole-state excitation method [38]. The enhancement of c_n , allowed by the χ^2 , yields very large neutron radii not confirmed in other experiments.

It was argued in Ref. [22] that the additional data needed to pinpoint the nuclear surface shape come from the radiochemical measurements. With an optical potential derived from zero range $\bar{N}N$ interactions, these data favored the halo type solution. Such conclusion is also supported here, and exemplified in Table V by the ^{124}Sn case. It also favors the halo type solution but the extracted $R_{rms}(n) - R_{rms}(p)$ are larger and closer to the hadron scattering results. The same effect occurs in the case of Pb nucleus. The favored neutron radius excess $R_{rms}(n) - R_{rms}(p) = 0.22(3)$ fm given in Table VI is 0.05 fm larger than the radius obtained with different optical potentials in Ref. [39]. There are two factors contributing to that: the first and the dominant one is the chamber data that enforces smaller $R_{n/p}$, and second the $a(r)$ given by nuclear models tends to be smaller at large distances. Due to both factors the neutron radius obtained from the X-ray data is slightly smaller than the radius obtained from the joint X-ray and radiochemical data.

IV. CONCLUSIONS

In this paper a step was taken to describe the antiprotonic atom data in a semi-phenomenological way. The best-fit optical potential was constrained by the atomic data from the \bar{p} hydrogen, deuterium and helium atoms. Additional information on the S wave isospin structure was extracted from the chamber low-energy \bar{p} data. All these constraints refer to the absorptive potentials. Following results have been obtained:

TABLE V: The $R_{rms}(n) - R_{rms}(p)$, in fm units, extracted from the X-ray data in antiprotonic Sn, Te, Zr and Ca atoms. The first column refers to charge density profile the second indicates the free parameter of the neutron density. As discussed in the text, the results obtained with charge density from Ref. [24] are the favored ones. The last column and the entries marked by * are extracted from the X-ray and radiochemical data.

ρ_{charge}		^{112}Sn	^{116}Sn	^{120}Sn	^{124}Sn	$^{124}\text{Sn}^*$
[24]	a_n	0.21(5)	0.22(4)	0.22(4)	0.23(4)	0.26(4)
2pF[23]	a_n	0.12(4)	0.15(4)	0.16(4)	0.21(4)	0.25(3)
2pF[23]	c_n	0.25(5)	0.31(6)	0.35(8)	0.42(7)	0.45(6)
		^{122}Te	^{124}Te	^{126}Te	^{128}Te	$^{128}\text{Te}^*$
[40]	a_n	0.10(7)	0.04(4)	0.12(5)	$0.08^{+0.07}_{-0.04}$	0.15(5)
		^{130}Te	$^{130}\text{Te}^*$	^{90}Zr	^{96}Zr	$^{96}\text{Zr}^*$
[40],[24]	a_n	0.10(5)	0.17(4)	$0.08^{+0.01}_{-0.04}$	0.12(3)	$0.16^{+0.06}_{-0.08}$
		^{40}Ca	^{42}Ca	^{44}Ca	^{48}Ca	$^{48}\text{Ca}^*$
[24]	a_n	-0.09(9)	0.01(6)	.02(6)	$0.09^{+0.06}_{-0.08}$	0.10(7)

TABLE VI: The $R_{rms}(n) - R_{rms}(p)$ differences extracted from antiprotonic ^{208}Pb atoms. The entries in parentheses [] give the corresponding χ^2 given mostly by the level shifts. Second line gives the difference of neutron and proton diffuseness parameters $a_{np} = a_n - a_p$

parameter	ρ_{charge} [23]	ρ_{charge} [24]
a_n	0.16(3) [10]	0.22(3)[10]
a_{np}	0.11	0.15
c_n	0.47(8) [3]	0.55(8)[3]

- A consistent description of the annihilation parameters in antiprotonic X-ray data, chamber data and the updated Paris potential model, which incorporates the $\bar{N}N$ scattering.
- This consistency allows to separate the S and P -wave contributions to the optical potential for antiprotons and estimate fairly precisely the ratio of $\bar{p}n$ and $\bar{p}p$ annihilation at very distant nuclear surfaces. The corresponding parameter $R_{n/p} = 0.86(4)$ averaged over a range of nuclei is obtained at these distances and it allows to discuss jointly the X-ray data and the radiochemical data.
- A definite energy dependence of the $\bar{N}N$ scattering amplitudes in the subthreshold region is indicated by the lightest atom data, chamber data and the $\bar{N}N$ Paris potential. For the S wave it is reflected in the widths of upper and lower levels in heavy atoms. For P waves there is an indication of a fairly narrow $\bar{N}N$ quasi-bound state. It is likely that such a state has sizable effect in a small sector of the radiochemical data taken on loosely bound protons. On the other hand, apart from the deuteron, the X-ray data offer no convincing evidence for such a state. New X-ray experiments performed with nuclei of small nucleon separation energies would be helpful to resolve this question.
- The \bar{p} X-ray data, although related to the nuclear surface, may supply important information on the neutron radii. However, these data taken by itself cannot tell precisely if the neutron excess forms an extended half-density radius, enlarged diffuseness or some specific correlation of both parameters. Jointly with the scattering and/or radiochemical data the \bar{p} results favor the neutron profiles of enlarged diffuseness.
- One important source of uncertainty in the description of the \bar{p} nucleus interactions is the real part of the optical potential and the related level shifts. It is complicated by the increasing evidence of $\bar{p}N$ quasi-bound states. Precise measurements of the atomic fine structure, in particular in very light atoms, would be very helpful to resolve this question.

APPENDIX A: THE GRADIENT POTENTIAL

The P wave collisions of N and \bar{N} , described in their center of mass system, involve the relative momentum $\mathbf{p} = (\mathbf{p}_N - \mathbf{p}_{\bar{N}})/2$. It generates the gradient potential given by expression (4) in the main text which contains the nucleon wave functions and their gradients. These are not easily reducible to the nuclear densities. Summation over nucleon states and calculations of the derivatives in eq.(4) yield involved expressions for V_G . The input uncertainties and experimental errors call for a simpler result. To obtain it let us remind that in the "upper" high angular momentum states $|n, l\rangle$ the level shifts ϵ and widths Γ are quite accurately given by

$$\epsilon - i\Gamma/2 \simeq \langle n, l | V^{opt} | n, l \rangle. \quad (\text{A1})$$

For such average values the gradient potential V_G may be expressed by a simpler formula [41]

$$\langle n, l | \hat{V}_G | n, l \rangle = \frac{2\pi}{\mu_{NN}} \frac{3}{4} a_P \int d\mathbf{u} g_P(\mathbf{u}) \int d\mathbf{r} \rho(\mathbf{r} - \mathbf{u}) \bar{D}^2 \Psi_{n,l}^2(\mathbf{r}) + |\Psi_{n,l}(\mathbf{r} - \mathbf{u})|^2 \Sigma_\alpha D^2 \varphi_\alpha^2(\mathbf{r}) + V^{mix} \quad (\text{A2})$$

where $\rho = \Sigma |\varphi_\alpha|^2$ is the nuclear density, $\Psi_{n,l}$ is the atomic wave function and

$$\bar{D}^2 \Psi_{n,l}^2(\mathbf{r}) = [\Psi'_{r,n,l}(r)^2 + \frac{l(l+1)}{r^2} \Psi_{r,n,l}^2(r)] \frac{1}{4\pi}, \quad (\text{A3})$$

$$D^2 \varphi_\alpha^2(\mathbf{r}) = [\varphi'_{r,\alpha}(r)^2 + \frac{L(L+1)}{r^2} \varphi_{r,\alpha}^2(r)] \frac{1}{4\pi}. \quad (\text{A4})$$

In these equations $\Psi_{r,n,l}$ denotes the radial part of the atomic wave functions in states of main quantum numbers n and angular momentum l . The nucleon angular momentum is denoted by L . Eqs.(A3) and (A4) are obtained with the "gradient formula" which splits the derivative into tangential and radial components. The two terms in eq.(4) which contain mixed $\vec{\nabla}_{\bar{p}} \vec{\nabla}_N$ gradients generate V^{mix} . The latter may be expressed by a formula obtained in Ref. [41],

$$\langle \hat{V}^{mix} \rangle = \frac{2\pi}{\mu_{NN}} \frac{3}{4} a_P \int d\mathbf{x} \int d\mathbf{y} [\vec{\nabla} \Psi_x^* \vec{\nabla} \Psi_x g_{xy} \rho_y + (\Psi_x^* \frac{\Delta}{2} \Psi_x + \frac{\Delta}{2} \Psi_x^* \Psi_x) g_{xy} \rho_y + (2i\mu_{NN})^2 \vec{j}_x g_{xy} \vec{j}_y] \quad (\text{A5})$$

A shorthand notation is used and arguments were put into indices i.e. $g_{xy} = g(\mathbf{x} - \mathbf{y})$, $\Psi_x = \Psi(\mathbf{x})$ etc. The first and the second term in this equation tend to cancel strongly. The last term, where \vec{j} denotes the nucleon and antiproton currents yields the main effect. For even A (spin zero) nuclei the tangential currents average to zero and one is left with the radial components which generate $\Psi_{r,n,l} \Psi'_{r,n,l} \varphi'_{r,\alpha} \varphi_{r,\alpha}$ contributions. However, in odd-A nuclei the tangential components in the last term introduce correlations of the atomic and nuclear currents. It leads to splitting of the atomic levels. Usually, this effect is small, but it may be magnified if both antiproton and the odd valence nucleon have high angular momenta.

Now some approximations are introduced to make the gradient potential applicable to practical calculations. For nucleons, the radial gradients are needed only at large distances. In this region one has, on average, $\varphi'_r \approx \varphi_r/2a$ where a is the surface thickness parameter. To account for the tangential gradient, the angular momentum factor $L(L+1)$ in eq.(A3) is averaged over the three uppermost nucleon shells given by simple shell model [42]. The gradients of atomic wave functions may be given explicitly for the circular orbits of interest. These functions are

$$\Psi_{r,n,l}(r) = N(n, l) r^l \exp(-r/Bn) F_{nucl}(r), \quad (\text{A6})$$

where N is a normalization, B is the Bohr radius and F_{nucl} describes the deformation of the Coulomb wave function due to short range (nuclear + finite charge) interactions. The dominant effect in F comes from the damping due to absorption. For the radial derivative one has $\Psi'_{r,n,l} = (l/r - 1/nB + F'/F) \Psi_{r,n,l}$ and the last term is calculated in a quasi-classical way in terms of $p_{WKB}(V) = \sqrt{2M_{\bar{N}}(E - V)}$ the value of local momentum of the antiproton inside the nucleus. One has $F'/F = ip_{WKB}(V_{centr} + V_{cul}) - ip_{WKB}(V_{centr} + V_{cul} + V^{opt})$ and numerically one finds that dropping the F'/F term altogether yields a minute change of the best fit parameters, making an overall χ^2 worse by 2.5. Also, it was found that a numerical calculation of $\partial\Psi/\partial r$ makes no substantial improvement.

The approximation (A2) is well fulfilled in the "upper" atomic orbits. Thus equation (A4) is used here to *define* the local equivalent to the nonlocal gradient V_G potential that gives the same expectation value in a given atomic orbital of a given atom. Expressions (A2,A3,A4) lead to a typical folded optical potential

$$\hat{V}_P(r) = \frac{2\pi}{\mu_{NN}} a_P \frac{3}{4} \int d\mathbf{u} f_P(\mathbf{u}) D_r^2 \rho(\mathbf{r} - \mathbf{u}) \quad (\text{A7})$$

where the effect of antiproton and nucleon momenta is now included into a function

$$D_r^2 = \left[\left| \frac{l}{r} - \frac{1}{nB} + F'/F \right|^2 + \frac{l(l+1)}{r^2} \right] + \left[\frac{1}{4a^2} + \frac{\langle L(L+1) \rangle}{r^2} \right] + \text{Re} \left(\frac{l}{r} - \frac{1}{nB} + F'/F \right) \frac{1}{a} \quad (\text{A8})$$

These approximations bring the optical potential back to the form given by the basic equation 1 in the main text. Now \hat{V}_P is given by eq.A7 summed over protons and neutrons. The interpretation of three terms in eq.A8 is fairly transparent. The first piece contains tangential and radial momenta of the orbital antiproton. It is the "localized" version of the gradient term used in mesonic atoms. The second term contains radial and tangential components of the nucleon momenta. The radial ones are expressed in terms of the nuclear density diffuseness parameter. The last piece is the mixed term which contains only the radial term as for spin zero systems the average product of tangential momenta vanishes. All together the nucleon momentum part contributes about one quarter of V^{opt} . On a phenomenological level it may be approximately included into the V_S potential term. The difference arises when one attempts to relate a_S and a_P to the scattering data. Another special effect of this nucleon term is due to its dependence on the nucleon angular momenta. Some enhancement arises in high L shells e.g. in Pb nucleus (12h protons and 14i neutrons in the valence shell). Unfortunately, the $L(L+1)$ averaging procedure contains some model dependence but the effect is moderate anyway, since the $\langle L(L+1) \rangle$ term constitutes less than 10% of the total D_r^2 . In practical calculations we used a smooth, approximate interpolation $\langle L(L+1) \rangle = 2 + (3Z/2 - 10)/4$. Rather slow but systematic increase of D_r^2 follows the rising atomic number Z . It is due to the increase in the L and l values. The impact of the nucleon $\langle L(L+1) \rangle$ term is also rather limited. Dropping it requires a change of a_P from the value $0.0 - i0.41 fm^3$ (line 3 in Table III) to the value $0.0 - i0.43 fm^3$ and the χ^2 increases by 4 units.

ACKNOWLEDGMENTS

We are grateful to Peter Ring for his interest in this work and for providing several nuclear density profiles. This work was supported by the Deutsche Forschungsgemeinschaft Bonn grant 436POL/17/8/04, and Polish Ministry of Science project 1 P03B 042 29

-
- [1] A. Trzcińska, J. Jastrzębski, T. Czosnyka, T. von Egidy, K. Gulda, F.J. Hartmann, J. Iwanicki, B. Ketzer, M. Kisielinski, B. Klos, W. Kurcewicz, P. Lubiński, P.J. Napiórkowski, L. Pieńkowski, W. Schmid, and E. Widmann, Nucl. Phys. **A692**, 176c(2001).
 - [2] P. Roberson, T. King, R. Kunselman, J. Miller, R.J. Powers, P.D. Barnes, R.A. Eisenstein, R.B. Sutton, W.C. Lam, C.R. Cox, M. Eckhouse, J.R. Kane, A.M. Rushton, W.F. Vulcan and R.E. Welsh, Phys. Rev. **C5**, 1954 (1977).
 - [3] Th. Köhler, P. Blüm, G. Büche, A.D. Hancock, H. Koch, A. Kreissl, H. Poth, U. Raich, D. Rochmann, G. Backenstoss, Ch. Findeisen, J. Repond, L. Tauscher, A. Nilsson, S. Carius, M. Suffert, S. Charalambus, M. Chardalas, S. Dedoussis, H. Daniel, T. von Egidy, F.J. Hartmann, W. Kanert, G. Schmidt, J.J. Reidy, M. Nicholas, and A. Wolf, Phys. Lett. **B176**, 327 (1986).
 - [4] D. Rohmann, H. Barth, A.D. Hancock, H. Koch, Th. Kohler, A. Kreissl, H. Poth, U. Raich, A. Wolf, and L. Tauscher, Z. Phys. **A325**, 261 (1986).
 - [5] M. Augsburger, D. Anagnostopoulos, G. Borchert, D. Chatellard, J. Egger, P. El-Khoury, H. Gorke, D. Gotta, P. Hauser, and P. Indelicato, Nucl. Phys. **A658**, 149 (1999).
 - [6] M. Augsburger, D. Anagnostopoulos, G. Borchert, D. Chatellard, J.-P. Egger, P. El-Khoury, H. Gorke, D. Gotta, P. Hauser, and P. Indelicato, Phys. Lett. **B461**, 417 (1999).
 - [7] D. Gotta, D. F. Anagnostopoulos, M. Augsburger, G. Borchert, C. Castelli, D. Chatellard, J. P. Egger, P. El-Khoury, H. Gorke, and P. Hauser, Nucl. Phys. **A660**, 283 (1999).
 - [8] M. Schneider, R. Bacher, P. Blüm, D. Gotta, K. Heitlinger, W. Kunold, D. Rohmann, J. Egger, L.M. Simons, and K. Elsner, Z.Phys. **A338**,217(1991)
 - [9] C. J. Batty, E. Friedman, and A. Gal, Phys. Rep. **287C**, 385 (1997).
 - [10] E. Fridman, A. Gal, and J. Mares, Nucl Phys. **A761**, 283(2005).
 - [11] R. Bizzari, P. Guidoni, F. Marcelija, F. Marzano, E. Castelli, and M. Sessa, Nuovo Cim. **22A**, 225 (1974); T.E. Kalogeropoulos, Phys. Rev. **D22**, 2585 (1980).
 - [12] F. Balestra, S. Bossolasco, M.P. Bussa, L. Busso, L. Ferrero, D. Panziera, G. Piragino, F. Tosello, R. Barbieri, G. Bendiscioli, A. Rotondi, P. Salvini, A. Venaglioni, A. Zenoni, Yu.A. Batusov, I.V. Falomkin, G.B. Pontecorvo, A.M. Rozhdestvensky, M.G. Sapozhnikov, V.I. Tretyak, C. Guaraldo, A. Maggiora, E. Lodi Rizzini, A. Haatuft, A. Halsteinslid, K. Myklebost, J.M. Olsen, F.O. Breivik, T. Jacobsen, and S.O. Sorensen, Nucl.Phys. **A491**,541(1989).
 - [13] B. El-Bennich, M. Lacombe, B. Loiseau, and R. Vinh Mau, Phys.Rev. **C59**,2313(1999); M. Lacombe *et al.* to be published.
 - [14] B. Loiseau and S. Wycech, Phys. Rev. **C72**,011001(2005).
 - [15] S. Wycech and B. Loiseau, LEAP05, AIP Conf.Series 796,131(2005).

- [16] S. Wycech, Nucl.Phys. **A692**,29c(2001).
- [17] J. Jastrzębski, H. Daniel, T. von Egidy, A. Grabowska, Y.S. Kim, W. Kurcewicz, P. Lubiński, G. Riepe, W. Schmid, A. Stolarz, and S. Wycech, Nucl. Phys. **A558**, 405c (1993).
- [18] P. Lubiński, J. Jastrzębski, A. Grochulska, A. Stolarz, A. Trzcińska, W. Kurcewicz, F.J. Hartmann, W. Schmid, T. von Egidy, J. Skalski, R. Smolańczuk, S. Wycech, D. Hilscher, D. Polster, and H. Rossner, Phys. Rev. Lett. **73**, 3199 (1994)
- [19] P. Lubiński, J. Jastrzębski, A. Trzcińska, W. Kurcewicz, F.J. Hartmann, W. Schmid, T. von Egidy, R. Smolańczuk, and S. Wycech, Phys. Rev. **C 57**, 2962 (1998);
- [20] R. Schmidt, F.J. Hartmann, T. von Egidy, T. Czosnyka, J. Iwani cki, J. Jastrzębski, M. Kisieliński, P. Lubiński, P. Napiorkowski, L. Pieńkowski, A. Trzcińska, J. Kulpa, R. Smolańczuk, S. Wycech, B. Kłos, K.Gulda, W. Kurcewicz, and E. Widmann, Phys. Rev. **C58**, 3195 (1998).
- [21] S. Wycech J. Skalski, R.Smolańczuk, J. Dobaczewski, and J.R. Rook, Phys. Rev. **C54**,1832(1996).
- [22] A. Trzcińska, J. Jastrzębski, P. Lubiński, F.J. Hartmann, R. Schmidt, T. von Egidy, B. Kłos, Phys. Rev. Lett. **87**, 082501 (2001).
- [23] H. de Vries, C. W. Jager and C. de Vries At. Data Nucl. Data Tab. **36**, 495 (1987), C. W. Jager, H. de Vries, and C. de Vries, *ibid.* **14**, 479 (1974)
- [24] G. Fricke, C. Bernhardt, K. Heilig, L. A. Schaller, L. Schellenberg, E. B. Shera, and C. W. Jager, *ibidem* **60**,177 (1995).
- [25] B. Loiseau and S. Wycech, Phys. Rev. **C63**,034003(2001).
- [26] R. Smolańczuk, private communication
- [27] G.A. Lalazissis, T. Niksic, D. Vretenar, and P. Ring, Phys.Rev. **C 71**,024312(2005)
- [28] D. Berdichevsky and U. Mosel, Nucl. Phys. **A388**, 229(1982).
- [29] S. Wycech, A.M. Green, and J.A. Niskanen, Phys. Lett. **B132**,308 (1985). S. Wycech and A.M. Green, Z. Phys. **A344**, 117 (1992).
- [30] F. Balestra, S. Bossolasco, M.P. Bussa, L. Busso, L. Ferrero, D. Panzieri, G. Piragino, F. Tosello, R. Barbieri, G. Bendiscioli, A. Rotondi, P. Salvini, A. Zenoni, Yu.A. Batusov, I.V. Falomkin, G.B. Pontecorvo, M.G. Sapozhnikov, V.I. Tretyak, C. Guaraldo, A. Maggiora, E. Lodi Rizzini, A. Haatuft, A. Halsteinslid, K. Myklebost, J.M. Olsen, F.O. Breivik, T. Jacobsen, and S.O. Sorensen, Nucl.Phys. **A491**, 572(1989).
- [31] J. Jastrzębski, A. Trzcińska, P. Lubiński, B. Kłos, F.J. Hartmann, T. von Egidy and S. Wycech, Int.Journ.Mod.Phys. **E13**, 343(2004).
- [32] A. Trzcińska, J. Jastrzębski, P. Lubiński, F. J. Hartmann, R. Schmidt, T. von Egidy and B. Kłos, Nucl. Instr. Meth. in Phys. Res. **A533**, 598 (2004).
- [33] R.J. Furnstahl, Nucl.Phys. **A706**,85(2002).
- [34] S. Wycech, AIP Conf. Proc. **793**, 201(2005).
- [35] V. E. Starodubsky and N.M. Hintz, Phys. Rev. **C49** 2118 (1994).
- [36] H.J. Koerner and J.P. Schiffer, Phys.Rev.Lett. **27**,1457 (1971) G. Mairle and G. Grabmayr, Eur.Phys.Journ. **A9**,913 (2000).
- [37] L. Ray, Phys.Rev. **C19**,1855(1979).
- [38] A. Krasznahorkay, M. Fujiwara, P. van Aarle, H. Akimune, I. Daito, H. Fujimura, Y. Fujita, M. N. Harakeh, T. Inomata, J. Janecke, S. Nakayama, A. Tamii, M. Tanaka, H. Toyokawa, W. Uijen, and M. Yosoi, Phys.Rev. Lett. **82**, 3216 (1999).
- [39] B. Kłos, *et al.* to be published.
- [40] E.B. Shera, H.M. Hoehn, G. Fricke, and G. Mallot, Phys.Rev. **C39**,195 (1989).
- [41] A. M. Green and S. Wycech, Nucl. Phys. **A467**, 744 (1987).
- [42] A. Bohr and B. Mottelson, *Nuclear Structure* (Benjamin, New York, 1969) p 224.